Geophysical Research Letters

Supporting Information for

A New Multi-Method Assessment of Stratospheric Sulfur Load from the Okmok II Caldera-Forming Eruption of 43 BCE

Ally Peccia[1,2], Yves Moussallam[1,2], Terry Plank[1,2], Kevin DallaSanta[3,4], Lorenzo Polvani[1,2,3], Alain Burgisser[5], Jessica Larsen[6] and Janet Schaefer[7]

[1]Lamont-Doherty Earth Observatory, Columbia University, Palisades, NY 10964

[2]Department of Earth and Environmental Sciences, Columbia University, Palisades, NY 10964

[3]Department of Applied Physics and Applied Mathematics, Columbia University, New York, NY, USA

[4]NASA Goddard Institute for Space Studies, New York, New York, USA

[5]Univ. Grenoble Alpes, Univ. Savoie Mont Blanc, CNRS, IRD, IFSTTAR, ISTerre, 38000 Grenoble, France

[6]Geophysical Institute, Department of Geosciences, Alaska Volcano Observatory, University of Alaska, Fairbanks, Fairbanks, AK, 99775, USA

[7]Alaska Volcano Observatory, State of Alaska Division of Geological and Geophysical Surveys, Fairbanks, AK, 99709, USA

Contents of this file

Text S1 to S7
Tables S1 to S3
Figures S1 to S4
References

Introduction

The supplementary information included here contains additional Text, Tables, and Figures which support the findings presented in the main article. We provide additional details on Okmok II petrography, GISS model setup and response, total mass and sulfur erupted estimates, sample preparation, and analytical conditions. Corresponding Text and Tables are grouped for easier reference.

Text S1. Calculated Sulfur Load for Okmok II Eruption

The erupted volume takes into account both pre-existing lithic material and the void fraction. Burgisser (2005) noted that PDCs contain 9-38 wt% dense lithic material, either derived from the vent, or emplaced in a previous eruption and then scoured by Okmok II pyroclastic flows. We correct for the median proportion of lithics (as measured in the massive facies) using:

$$M_v = V_d f \rho_a (1 - W_l) \qquad (1)$$

where V_d is the total volume of pyroclastic deposits, f is the deposit void fraction, ρ_a is the average density of PDC juvenile clasts, W_l is the mass fraction of lithics, and M_v is the mass of magma erupted. Burgisser (2005) measured an average clast density of 1450 kg/m^3, and a median lithic proportion of 26 wt % in PDCs. The deposits themselves are well packed and highly polydisperse; their void fraction is thus above the maximum packing of monodisperse spheres (0.67). This leads us to assume an average void fraction of 0.8±0.1. Given a total volume of 50 km^3, we calculate a total erupted magma mass of $4.29 \pm 1.01 \times 10^{13}$ kg.

Table S1. Calculated Sulfur Load for Okmok II Eruption

Parameter	Value	Uncertainty	Reference/Method
Erupted volume	50 km^3	10 km^3	1
Mass of magma erupted	4.29*10^{13} kg	1.01*10^{13} kg	2
Crystal fraction	1.7%	1.8%	3
C(S) inclusion	1606 ppm	160 ppm	4
C(S) matrix	127 ppm	23 ppm	5
Total Erupted S	62 Tg S	16 Tg S	6

Notes:

1. Erupted volume derives from Burgisser (2005) and is based on field measurements of deposit thickness and the total volume of the Okmok II caldera (50 ± 10 km3). (See Fig. S3).
2. Mass of magma erupted is estimated from the total erupted volume with an average deposit density of 1450 kg/m^3, corrected for pore space and 26 wt% lithic fragments observed by Burgisser (2005). The uncertainty reflects ±10 km^3 uncertainty in total deposit volume.
3. Median crystal weight fraction observed in the massive facies of PDC deposits, re-normalized to 100 with the removal of lithic weight fraction. 1.8% uncertainty reflects standard deviation across samples measured.
4. Maximum sulfur measured via ionprobe in AOK147plag-melt inclusion (Fig. 1b); uncertainty reflects 10% uncertainty in ionprobe measurement.
5. Average and standard deviation of all matrix glass in this study, not including glass adhered to phenocrysts.
6. Using equation in text for petrological method (Devine et al., 1984), uncertainty from error propagation.

Text S2. Petrologic sulfur loads for large historical eruptions
The Table below outlines the sulfur loads, methods and references for different eruptions, as illustrated in Fig. 3.

Table S2. Petrologic sulfur loads for large historical eruptions

Eruption	**Petrologic S load (Tg)**	**Method**	**Source**
TBJ Ilopango (431 CE)	90	90-200 Tg with basaltic parent incorporated, recently redated to 431 CE	Smith, et al. [2020]; Dull, et al. [2019]
Huayanaputina (1600 CE)	26-55	Unusually large S load from interaction with hydrothermal system	Dietterich and Silva [2010]; Costa, et al. [2003]
Kuwae (1452 CE)	7-13 from silicate + 43-86 from fluid phase	Modern petrologic with discussion of classic petrologic silicate	Witter and Self [2007]
Laki (1783 CE)	61	Classic petrologic, melt inclusions	Thordarson, et al. [1996];Thordarson and Self [2003]
Eldgja (934 CE)	110	Classic petrologic	Thorsdarson, et al. [2001]
Agung (1963 CE)	3.5	Classic petrologic	Self and King [1998]
Paektu (946 CE)	45	Modern petrologic (fluid phase contribution, basaltic parent)	Iacovino, et al. [2016]
Tambora (1815 CE)	74	Modern petrologic	Pouget, et al. [2023]; Gertisser, et al. [2012]
Samalas (1257 CE)	79	Modern petrologic (fluid and basaltic parent)	Vidal, et al. [2016]
Santa Maria (1902 CE)	4	Classic petrologic, melt inclusions	Scalliet, et al. [1998]
Minoan (1645 BCE)	36	Modern petrologic (fluid phase contribution)	Cadoux, et al. [2015]
Krakatau (1883 CE)	7	Modern petrologic (fluid phase contribution)	Scalliet, et al. [1998]; Mandeville, et al. [1996]
Pinatubo (1991 CE)	9	TOMS, modern petrologic re-evaluation including contribution from fluid phase	Guo, et al. [2004]; Gerlach, et al. [1996]

Text S3. Sample Description and Location

Samples were chosen based on the locations and compositions given in Larsen, et al. (2007) and Burgisser (2005). The geochemical composition of the tephra recovered in the GISP2 ice core aligns most closely with samples of the andesite fall and PDC deposits, and so we chose samples from these deposits for study (Andesite fall samples 01JLOK54D and 98JLOK6H, and PDC samples AOK142 and AOK147). Furthermore, clasts most likely to have experienced a high quench rate (andesite lapilli airfall on Umnak and PDC scoria lapilli from Unalaska Island) were prioritized, as fast cooling tends to minimize diffusive water loss through host minerals and subsequent crystallization or leakage of melt inclusions (Fig. 1a; Lloyd et al., 2012). After crushing and sieving, crystals were picked from the 250 μm – 1 mm fraction of the four samples indiscriminately of mineral type. Melt inclusions were visually identified in plagioclase, olivine, and pyroxene crystals for mounting and polishing. Candidate crystals were oriented and mounted singly on one-inch glass slides using heated Crystalbond mounting adhesive, then polished until melt inclusions were intersected, and imaged to assure that melt inclusions were glassy, fully enclosed and not cracked (Fig. 1d).

Table S3. Sample locations

Sample	Description	Latitude	Longitude
01JLOK54D (IGSN: 10.58052/IEAVO05BV)	Okmok Volcano: 2050 BP Andesite Fall scoria; Antler Creek	53.45186	-167.98606
98JLOK6H (IGSN: 10.58052/IEAVO0420)	2050 BP coarse andesite composition fall deposit. Smaller grain size scoria samples. Aphyric. No embedded lithics.	53.38113	-167.97003
AOK142 (IGSN: 10.58052/IEAVO05BW)	Base of PDC deposit on Unalaska, -2ϕ sieve fraction	53.35493	-167.75318
AOK147 (IGSN: 10.58052/IEAVO05BX)	Top of PDC deposit from Unalaska, 0.5ϕ sieve fraction	53.31795	-167.69947

Text S4. Analytical conditions

Electron microprobe measurements of major elements and sulfur concentrations in host crystals, melt inclusions, and matrix glasses were analyzed at the American Museum of Natural History Electron Microprobe Facility on a 5-spectrometer Cameca SX5-Tactis over three sessions between February 2021 and March 2022. Major elements were analyzed using a 10 nA beam current, 10 μm spot size, and 15 keV accelerating voltage (4 nA for Na). Volatile elements S and Cl were analyzed using a 40 nA beam current, 10 μm spot size, and 15 keV accelerating voltage.

SIMS (secondary ionization mass spectrometry) ion microprobe analysis of volatiles (H_2O, CO_2, Cl, F, and S) in selected inclusions and matrix glasses were carried out on the Cameca 7f io probe at the California Institute of Technology. A primary beam of Cs ions (3-4 nA) accelerated to 9 kV was used to create a pre-sputtered spot size of 15x15 μm.

The central 10 x 10 μm area was then analyzed using a 100 μm field aperature. Oxygen-normalized ratios were calibrated using DTM basaltic glass standards (Hauri et al., 2002), and all calibration lines were highly linear (R>0.98; Supplementary Data File).

Text S5. Petrography
The petrography of the Okmok II eruptive products is originally described in Larsen et al. (2007). While all phases were notably crystal-poor, assemblages include plagioclase, hypersthene, augite, and titano-magnetite in the rhyodacite fall, plagioclase, hypersthene, and titano-magnetite in the andesite fall. The basaltic andesite PDC phase includes plagioclase, hypersthene, augite, titano-magnetite, and sparse olivine. Both the andesite fall and basaltic andesite PDCs contain common plagioclase-dominate crystal clots with associated pyroxenes, Fe-Ti oxides, and olivine. Plagioclase is the most abundant mineral in all phases and is present in composition from An30-95, in approximately three populations: ~An30, ~An60, >An90. Larsen et al. (2007) note abundant plagioclase and pyroxene microlites in the basaltic andesite groundmass.

The phenocrysts analyzed in this study include plagioclase of composition An38-86 and olivine of Fo38-87, with pyroxene and magnetite also noted in studied samples. Plagioclase composition falls within the range described by Larsen et al. (2007), though tend to cluster in two groups from An81-86 and An38-54. Olivine composition appears to fall into a high Mg group from Fo72-87 and a low Mg group from Fo38-65. Abundant microlites of plagioclase and pyroxene were observed in matrix glasses from both the andesite fall and PDC samples.

Text S6. Description of Melt Inclusion Populations and Justification for Parental PDC Sulfur Concentration Suggested
The sulfur concentrations in a suite of 19 melt inclusions from Okmok II range from 152 to 1606±160 (10% relative uncertainty in ionprobe analysis) ppm S in melt compositions that span from basaltic to rhyolitic (51-65 wt% SiO_2). Sulfur concentration generally decreases with increasing SiO_2 and K_2O content (Fig. 1b), consistent with crystallization during ascent and degassing (and sulfide partitioning). The matrix glass composition is comparatively less diverse, ranging from 57-61 wt% SiO_2 with an average sulfur concentration of 127 ±23 ppm S (average of n = 23 glasses ± 1 standard deviation; Supplementary Data File). Three populations were identified based on melt inclusion (MI) and host phenocryst composition. The most mafic melt inclusions (50-54 wt% SiO_2, n=4) are hosted in high-Mg olivine (Fo72-87) that represent a more primitive magma than Okmok II whole rocks.

The second population of melt inclusions (n=5) reflects the bulk composition of magma erupted in Okmok II as PDCs, with a basaltic andesite composition (54.5-57 wt% SiO_2) hosted in high anorthite plagioclase (An86-81) and olivine (Fo72). The Waters and Lange (2015) plagioclase hygrometer and olivine-liquid partitioning relationship described in Toplis (2004) suggests the basaltic andesite PDC whole rock (which is largely aphyric) is in equilibrium with ~An80 and ~Fo70, consistent with melt inclusion hosts of this basaltic andesite population. Furthermore, calculated equilibrium for specific melt inclusion compositions in this population shows they are in equilibrium with their An86-

81 hosts at 2.3wt% H_2O, consistent with in-situ measurement of H_2O concentration via SIMS. This population also hosts inclusions with the highest sulfur concentrations, ranging from 1089-1606 ppm S. Some of these inclusions are hosted in a PDC sample (AOK147), while others are hosted in an andesite sample erupted prior (6H).

The third population of melt inclusions (n=11) includes evolved melt compositions typical of the rhyodacite and andesite fall units (59-65 wt% SiO_2) and are entrapped in sodic plagioclase phenocrysts (An38-54) and low-Mg olivine (Fo38 and Fo65). These melt inclusions contain an average sulfur concentration of 324 ± 21 ppm S, indicating degassing and crystallization upon ascent and sequestration in sulfides (Fig. 1b, c).

The melt inclusion populations identified match well with the stratigraphically observed eruptive sequence of rhyodacitic ash fall to voluminous basaltic andesite PDCs following caldera collapse (Fig. 1a, b). Further, the more evolved population of inclusions was observed primarily in phenocrysts recovered from andesite fall deposits, while the less evolved and primitive melt inclusions were found in PDC samples (Fig. 1b, c). The matrix glasses measured by McConnell et al. (2020) show a clear distinction between those from their andesite sample (higher in SiO_2 and lower in CaO) and those from their PDC sample (Fig. 1b). The matrix glasses studied here did not show such a clear distinction, with most compositions at the silicic end of the range observed by McConnell, et al. (2020) (Fig. 1b, c). Given that the GISP2 tephra are analyses of matrix glass, the best match is the PDC matrix glass from McConnell et al. (2020). This provides a strong link between the GISP2 tephra and the Okmok II PDC magma. Although the whole rock PDCs may include lithic material (most of which is aphyric basalt, Burgisser, 2005), the composition of whole-rock PDCs varies little between samples with a significant proportion of lithics versus those described as having no lithics. Thus, the more mafic (lower SiO_2 and higher CaO) composition of PDC whole rocks compared to the PDC matrix glass generally reflects degassing-driven crystallization of microlites (Fig. 1b, c).

Text S7. GISS model setup

The model was configured with a coupled ocean, prescribed atmospheric composition (except for water vapor), and pre-industrial conditions. As in McConnell et al. (2020), the Easy Volcanic Aerosol module (EVA, Toohey et al. 2016) was used to generate volcanic aerosol forcings at 10, 38, and 62 Tg S (spanning the range for our own estimates and that published in McConnell et al., 2020). We provided EVA with Okmok's latitude of 53.4 N (note McConnell et al. 2020 use 54.4 N) and a hemispheric asymmetry parameter of 11.19 (Sigl et al. 2022), which reflects the larger aerosol loading in the Northern Hemisphere. The aerosol radius was set to post-Pinatubo observations, as radii at higher sulfate injection amplitudes are uncertain (McGraw et al. in review). We simulated eruptions occurring on January 1. For each of the three forcing amplitudes, we ran a 10-member ensemble of simulations, with different initial conditions taken from the control run. We defined the "response" to the eruptions as ensemble average departure from the control run. We repeated the ensemble with eruptions occurring on July 1 to determine whether the eruption season alters the climate response.

Data Set S1. Major element composition and volatile content of melt inclusions, host crystals, and matrix glasses from the Okmok II eruption, measured via EMPA and SIMS. The dataset is available freely to download via the EarthChem database:

Peccia, A., Moussallam, Y., & Plank, T. (2023). Melt inclusion and matrix glass data from the 43 BCE eruption of Okmok Volcano (Version 1.0). Interdisciplinary Earth Data Alliance (IEDA). https://doi.org/10.26022/IEDA/112955

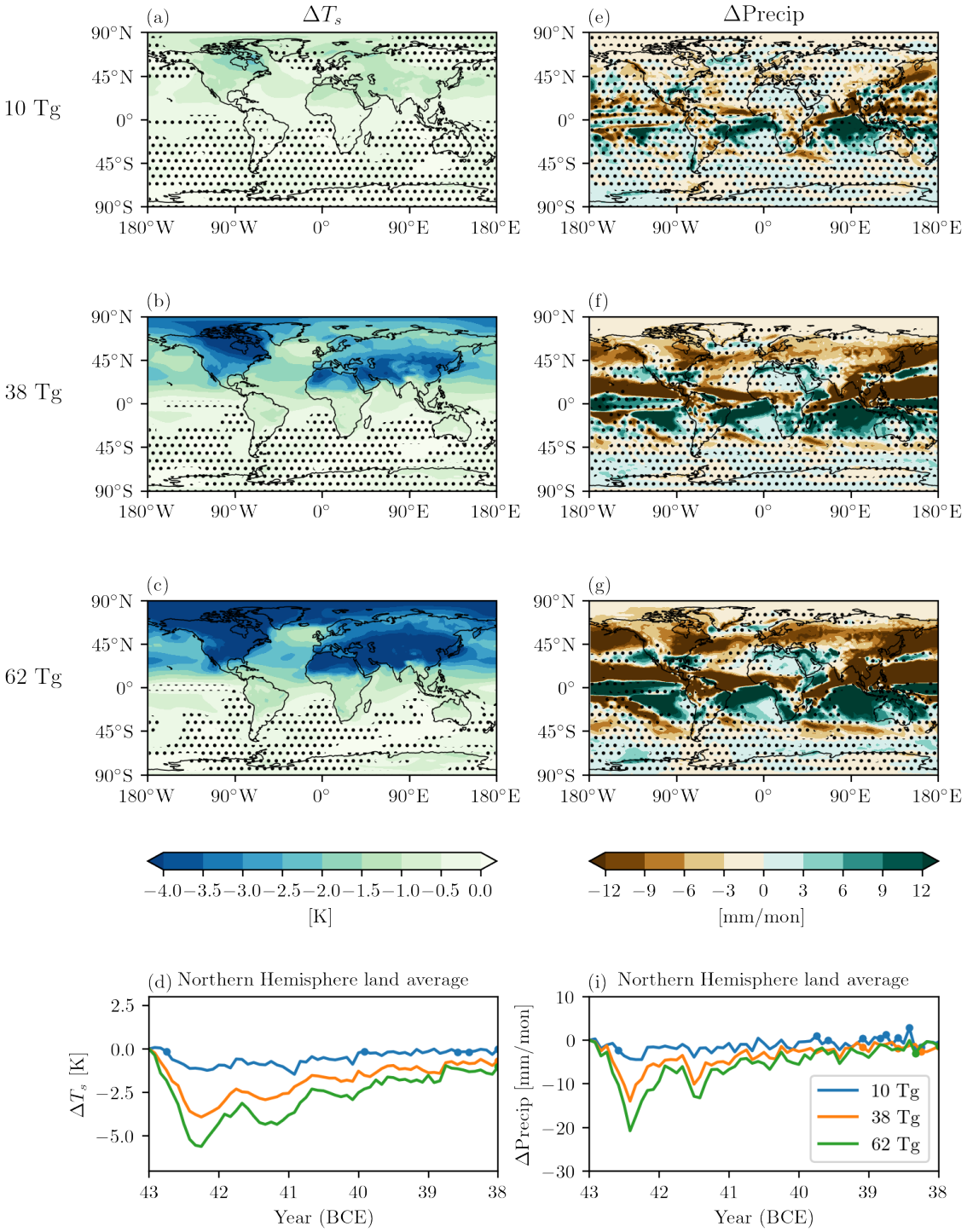

Figure S1. As in Figure 2, but rows 1–3 are global, and row 4 is averaged over Northern Hemisphere land. The contour intervals are saturated for consistency with Figure 2.

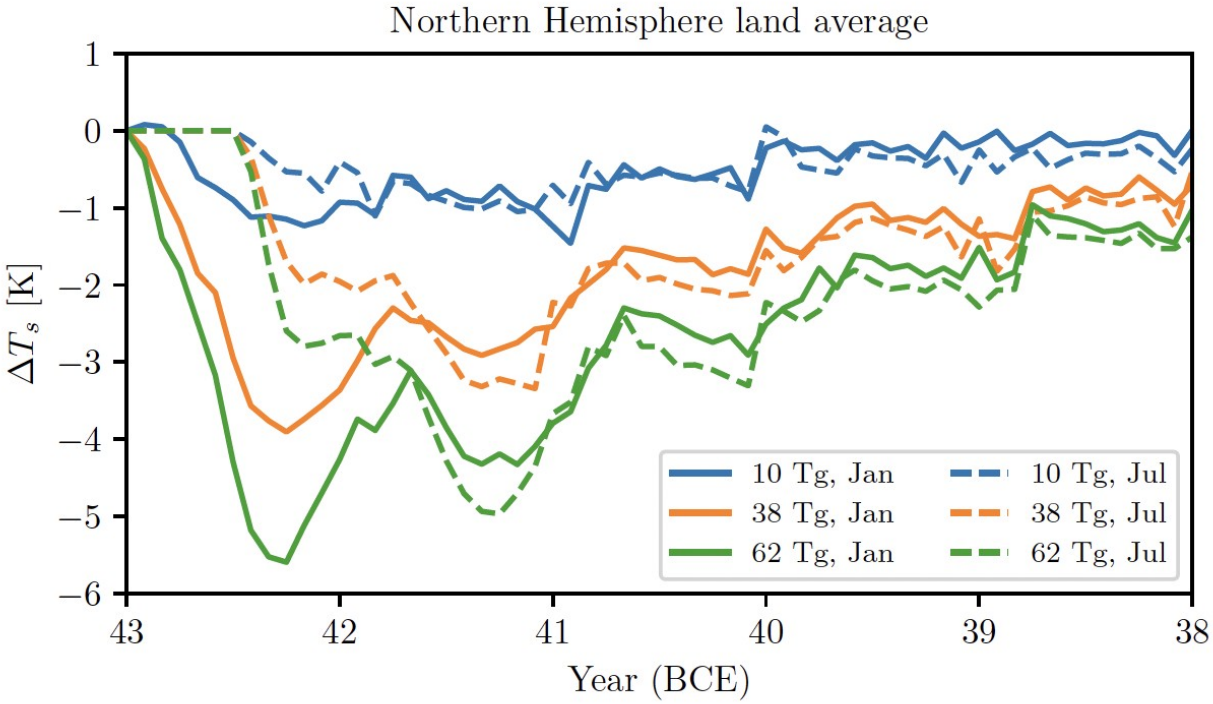

Figure S2. Time-evolving surface temperature responses to Okmok II, averaged over Northern Hemisphere land, for each sulfate amplitude and eruption month. Each line is an average of 10 members. Significance is omitted for clarity.

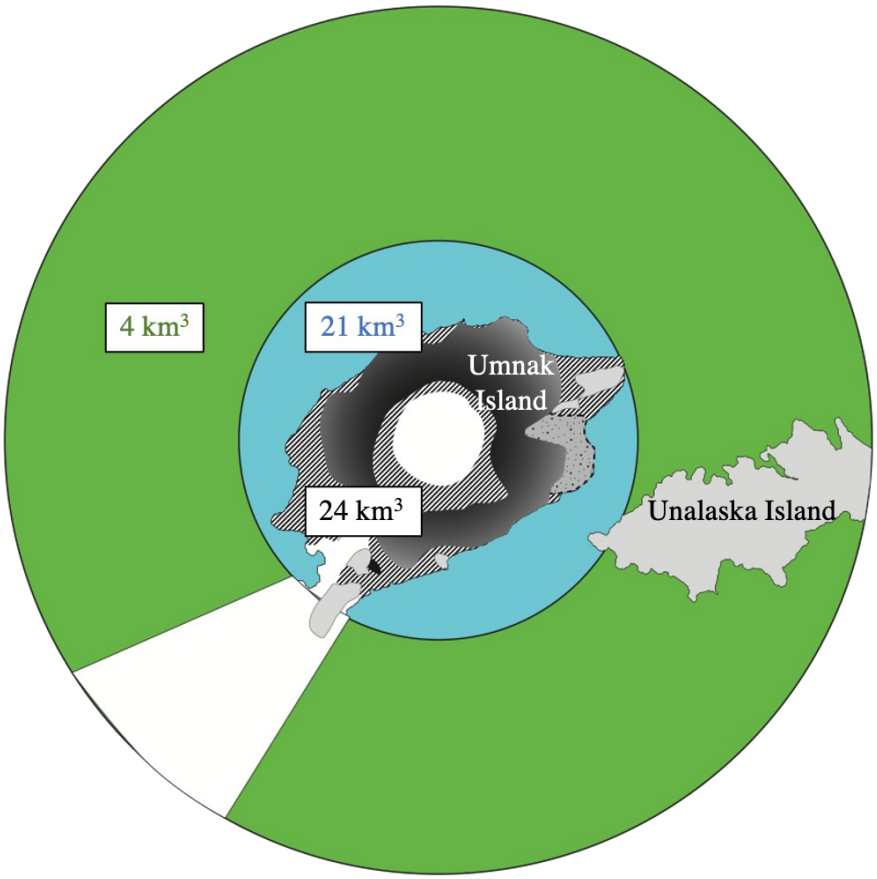

Figure S3. Map of Umnak and Unalaska Island and surrounding area, used to estimate PDC volume. The PDCs in the inner ring (blue) are assumed to yield the same thickness as the massive facies measured on the shores of Umnak Island (15 meters). The area in the outer ring (green) is assumed to be covered by the same thickness as the weakly stratified facies deposited on the proximal coast of Unalaska Island (70 cm). Deposits observed on land total to a volume of 24 km^3, while deposits emplaced underwater are estimated to comprise 25 km^3 (area in blue: 21 km^3 assuming 10 m thickness, area in green: 4 km^3 assuming 70 cm thickness). The sum is consistent with the volume of the Okmok II caldera (50 +/- 10 km^3, Burgisser (2005). The dark gray shading indicates regions where the massive facies of PDC deposits on land are >10 m thick and the hatched regions where the deposits are < 10 m.

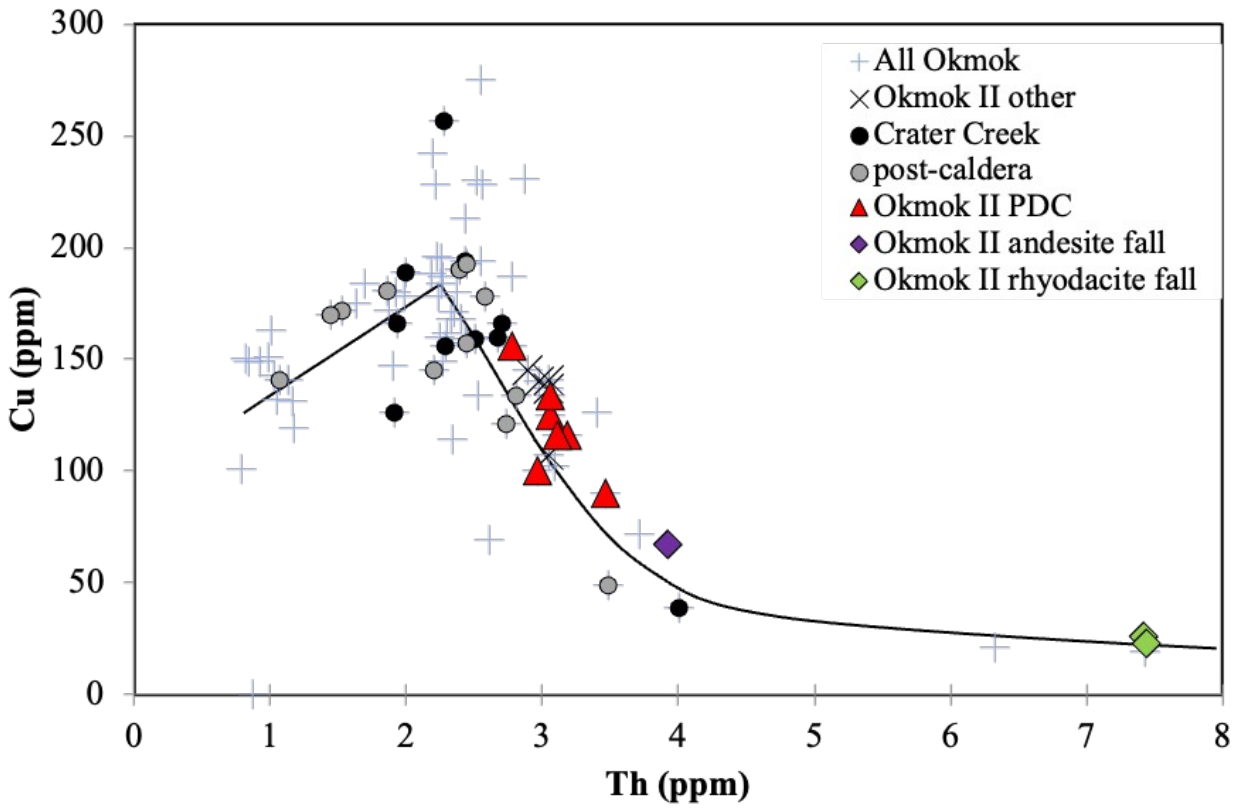

Figure S4. Copper concentrations measured in Okmok whole rocks from the Okmok II PDC, andesite fall, and rhyodacite fall phases, in addition to Okmok units associated with activity pre- and post-eruption. Some sulfide inclusions were found in olivine (Fo72) from the Okmok II andesite fall unit, and a decrease in Cu in evolved Okmok whole rocks (with Th > 2.5 ppm) requires sulfide saturation (line drawn by eye). Copper depletion in evolved whole rocks indicates sulfide saturation near the whole-rock composition of the PDCs. Thus, we make no correction for sulfides in determining the total sulfur load. Whole rock trace element concentrations were measured via ICP-MS and retrieved from AVO's Geochemical Data Repository (Okmok II) or published in Finney, et al. 2008 (Crater Creek and post-caldera).

References

Burgisser, A. (2005). Physical volcanology of the 2,050 bp caldera-forming eruption of Okmok volcano, Alaska. *Bulletin of Volcanology*, *67*(6), 497–525. https://doi.org/10.1007/s00445-004-0391-5

Cadoux, A., Scaillet, B., Bekki, S., Oppenheimer, C., & Druitt, T. H. (2015). Stratospheric Ozone destruction by the Bronze-Age Minoan eruption (Santorini Volcano, Greece). *Scientific Reports*, *5*(1), Article 1. https://doi.org/10.1038/srep12243

Devine, J. D., Sigurdsson, H., Davis, A. N., & Self, S. (1984). Estimates of sulfur and chlorine yield to the atmosphere from volcanic eruptions and potential climatic effects. *Journal of Geophysical Research: Solid Earth*, *89*(B7), 6309–6325. https://doi.org/10.1029/JB089iB07p06309

Dietterich, H., & de Silva, S. (2010). Sulfur yield of the 1600 eruption of Huaynaputina, Peru: Contributions from magmatic, fluid-phase, and hydrothermal sulfur. *Journal of Volcanology and Geothermal Research*, *197*(1), 303–312. https://doi.org/10.1016/j.jvolgeores.2010.01.003

Dull, R. A., Southon, J. R., Kutterolf, S., Anchukaitis, K. J., Freundt, A., Wahl, D. B., Sheets, P., Amaroli, P., Hernandez, W., Wiemann, M. C., & Oppenheimer, C. (2019). Radiocarbon and geologic evidence reveal Ilopango volcano as source of the colossal 'mystery' eruption of 539/40 CE. *Quaternary Science Reviews*, *222*, 105855. https://doi.org/10.1016/j.quascirev.2019.07.037

Finney, B., Turner, S., Hawkesworth, C., Larsen, J., Nye, C., George, R., Bindeman, I., & Eichelberger, J. (2008). Magmatic Differentiation at an Island-arc Caldera: Okmok Volcano, Aleutian Islands, Alaska. *Journal of Petrology*, *49*(5), 857–884. https://doi.org/10.1093/petrology/egn008

Gerlach, T. M., Westrich, H. R., Symonds, R. B., Newhall, C. G., & Punongbayan, R. S. (1996). Pre–eruption vapor in magma of the climactic Mount Pinatubo eruption: Source of the giant stratospheric sulfur dioxide cloud. In *Fire and Mud. Eruptions and Lahars of Mount Pinatubo, Philippines* (pp. 415–434). University of Washington Press.

Gertisser, R., Self, S., Thomas, L. E., Handley, H. K., Van Calsteren, P., & Wolff, J. A. (2012). Processes and Timescales of Magma Genesis and Differentiation Leading to the Great Tambora Eruption in 1815. *Journal of Petrology*, *53*(2), 271–297. https://doi.org/10.1093/petrology/egr062

Guo, S., Bluth, G. J. S., Rose, W. I., Watson, I. M., & Prata, A. J. (2004). Re-evaluation of SO2 release of the 15 June 1991 Pinatubo eruption using ultraviolet and infrared satellite sensors. *Geochemistry, Geophysics, Geosystems*, *5*(4). https://doi.org/10.1029/2003GC000654

Iacovino, K., Ju-Song, K., Sisson, T., Lowenstern, J., Kuk-Hun, R., Jong-Nam, J., Kun-Ho, S., Song-Hwan, H., Oppenheimer, C., Hammond, J. O. S., Donovan, A., Liu, K. W., & Kum-Ran, R. (2016). Quantifying gas emissions from the "Millennium Eruption" of Paektu volcano, Democratic People's Republic of Korea/China. *Science Advances*, *2*(11), e1600913. https://doi.org/10.1126/sciadv.1600913

Larsen, J. F., Neal, C., Schaefer, J., Beget, J., & Nye, C. (2007). Late Pleistocene and Holocene Caldera-Forming Eruptions of Okmok Caldera, Aleutian Islands,

Alaska. In *Volcanism and Subduction: The Kamchatka Region* (pp. 343–364). American Geophysical Union (AGU). https://doi.org/10.1029/172GM24

Marshall, L. R., Schmidt, A., Johnson, J. S., Mann, G. W., Lee, L. A., Rigby, R., & Carslaw, K. S. (2021). Unknown Eruption Source Parameters Cause Large Uncertainty in Historical Volcanic Radiative Forcing Reconstructions. *Journal of Geophysical Research: Atmospheres*, *126*(13), e2020JD033578. https://doi.org/10.1029/2020JD033578

McConnell, J. R., Sigl, M., Plunkett, G., Burke, A., Kim, W. M., Raible, C. C., Wilson, A. I., Manning, J. G., Ludlow, F., Chellman, N. J., Innes, H. M., Yang, Z., Larsen, J. F., Schaefer, J. R., Kipfstuhl, S., Mojtabavi, S., Wilhelms, F., Opel, T., Meyer, H., & Steffensen, J. P. (2020). Extreme climate after massive eruption of Alaska's Okmok volcano in 43 BCE and effects on the late Roman Republic and Ptolemaic Kingdom. *Proceedings of the National Academy of Sciences*, *117*(27), 15443–15449. https://doi.org/10.1073/pnas.2002722117

Peccia, A., Moussallam, Y., & Plank, T. (2023). Melt inclusion and matrix glass data from the 43 BCE eruption of Okmok Volcano (Version 1.0). Interdisciplinary Earth Data Alliance (IEDA). https://doi.org/10.26022/IEDA/112955

Pouget, M., Moussallam, Y., Rose-Koga, E., & Sigurdsson, H. (2023). A reassessment of the sulfur, chlorine and fluorine atmospheric loading during the 1815 Tambora eruption. Bulletin of Volcanology. https://doi.org/10.1007/s00445-023-01683-8

Scaillet, B., Clemente, B., Evans, B. W., & Pichavant, M. (1998). Redox control of sulfur degassing in silicic magmas. *Journal of Geophysical Research: Solid Earth*, *103*(B10), 23937–23949. https://doi.org/10.1029/98JB02301

Self, S., & King, A. J. (1996). Petrology and sulfur and chlorine emissions of the 1963 eruption of Gunung Agung, Bali, Indonesia. *Bulletin of Volcanology*, *58*(4), 263–285. https://doi.org/10.1007/s004450050139

Self, S., Gertisser, R., Thordarson, T., Rampino, M. R., & Wolff, J. A. (2004). Magma volume, volatile emissions, and stratospheric aerosols from the 1815 eruption of Tambora. Geophysical Research Letters, 31(20). https://doi.org/10.1029/2004GL020925

Smith, V. C., Costa, A., Aguirre-Díaz, G., Pedrazzi, D., Scifo, A., Plunkett, G., Poret, M., Tournigand, P.-Y., Miles, D., Dee, M. W., McConnell, J. R., Sunyé-Puchol, I., Harris, P. D., Sigl, M., Pilcher, J. R., Chellman, N., & Gutiérrez, E. (2020). The magnitude and impact of the 431 CE Tierra Blanca Joven eruption of Ilopango, El Salvador. *Proceedings of the National Academy of Sciences*, *117*(42), 26061–26068. https://doi.org/10.1073/pnas.2003008117

Thordarson, T., Miller, D. J., Larsen, G., Self, S., & Sigurdsson, H. (2001). New estimates of sulfur degassing and atmospheric mass-loading by the 934 AD Eldgjá eruption, Iceland. *Journal of Volcanology and Geothermal Research*, *108*(1), 33–54. https://doi.org/10.1016/S0377-0273(00)00277-8

Thordarson, T., & Self, S. (2003). Atmospheric and environmental effects of the 1783–1784 Laki eruption: A review and reassessment. *Journal of Geophysical Research: Atmospheres*, *108*(D1), AAC 7-1-AAC 7-29. https://doi.org/10.1029/2001JD002042

Thordarson, T., Self, S., Óskarsson, N., & Hulsebosch, T. (1996). Sulfur, chlorine, and fluorine degassing and atmospheric loading by the 1783–1784 AD Laki (Skaftár

Fires) eruption in Iceland. *Bulletin of Volcanology*, *58*(2), 205–225. https://doi.org/10.1007/s004450050136

Toohey, M., Stevens, B., Schmidt, H., & Timmreck, C. (2016). Easy Volcanic Aerosol (EVA v1.0): An idealized forcing generator for climate simulations. *Geoscientific Model Development*, *9*(11), 4049–4070. https://doi.org/10.5194/gmd-9-4049-2016

Toplis, M. J. (2005). The thermodynamics of iron and magnesium partitioning between olivine and liquid: criteria for assessing and predicting equilibrium in natural and experimental systems. Contributions to Mineralogy and Petrology, 149(1), 22–39. https://doi.org/10.1007/s00410-004-0629-4

Vidal, C. M., Métrich, N., Komorowski, J.-C., Pratomo, I., Michel, A., Kartadinata, N., Robert, V., & Lavigne, F. (2016). The 1257 Samalas eruption (Lombok, Indonesia): The single greatest stratospheric gas release of the Common Era. *Scientific Reports*, *6*(1), 34868. https://doi.org/10.1038/srep34868

Waters, L. E., & Lange, R. A. (2015). An updated calibration of the plagioclase-liquid hygrometer-thermometer applicable to basalts through rhyolites. American Mineralogist, 100(10), 2172–2184. https://doi.org/10.2138/am-2015-5232

Witter, J. B., & Self, S. (2007). The Kuwae (Vanuatu) eruption of AD 1452: Potential magnitude and volatile release. *Bulletin of Volcanology*, *69*(3), 301–318. https://doi.org/10.1007/s00445-006-0075-4